

# Mechanism of Excellent Photoelectric Characteristics in Mixed-Phase ZnMgO Ultraviolet Photodetectors with Single Cutoff Wavelength

Ming-Ming Fan,<sup>†,‡,§</sup> Ke-Wei Liu,<sup>\*,†</sup> Xing Chen,<sup>†</sup> Xiao Wang,<sup>†,‡</sup> Zhen-Zhong Zhang,<sup>†</sup> Bing-Hui Li,<sup>†</sup> and De-Zhen Shen<sup>\*,†</sup>

<sup>†</sup>State Key Laboratory of Luminescence and Applications, Changchun Institute of Optics, Fine Mechanics and Physics, Chinese Academy of Sciences, Dongnanhu Road 3888, Changchun, 130033, People's Republic of China

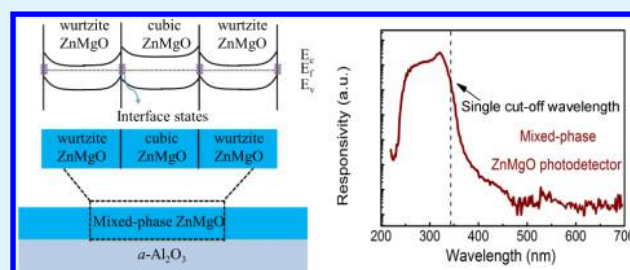
<sup>‡</sup>University of Chinese Academy of Sciences, Beijing, 100049, People's Republic of China

<sup>§</sup>College of Physics and Optoelectronics, Taiyuan University of Technology, Taiyuan, 030024, People's Republic of China

## S Supporting Information

**ABSTRACT:** Mixed-phase ZnMgO (m-ZMO) thin films with a single absorption edge tuning from  $\sim 3.9$  to  $\sim 4.8$  eV were realized on *a*-face sapphire (*a*-Al<sub>2</sub>O<sub>3</sub>) by plasma-assisted molecular beam epitaxy. The small lattice mismatch of both ZnO and MgO with *a*-Al<sub>2</sub>O<sub>3</sub> should be responsible for the single and controllable absorption edge. Metal–semiconductor–metal (MSM) photodetectors were fabricated based on these m-ZMO films, and the devices have the single cutoff wavelength, which can be tuned from 335 to 275 nm. These devices possess low dark current (78 pA for m-Z<sub>0.67</sub>M<sub>0.33</sub>O, 11 pA for m-Z<sub>0.59</sub>M<sub>0.41</sub>O, and 4 pA for m-Z<sub>0.39</sub>M<sub>0.61</sub>O at 40 V) and high responsivity (434 A/W for m-Z<sub>0.67</sub>M<sub>0.33</sub>O, 89.8 A/W for m-Z<sub>0.59</sub>M<sub>0.41</sub>O, and 3.7 A/W for m-Z<sub>0.39</sub>M<sub>0.61</sub>O at 40 V). Further response study reveals that the 90–10% decay time of m-Z<sub>0.67</sub>M<sub>0.33</sub>O, m-Z<sub>0.59</sub>M<sub>0.41</sub>O, and m-Z<sub>0.39</sub>M<sub>0.61</sub>O is around 37, 30, and 0.7 ms, respectively. Large amounts of heterojunction interfaces between wurtzite ZMO and cubic rock-salt ZMO could be responsible for the low dark current and high responsivity of our mixed-phase devices. The excellent comprehensive performance of m-ZMO UV photodetectors on *a*-Al<sub>2</sub>O<sub>3</sub> suggests that m-ZMO UV photodetectors should have great applied potential.

**KEYWORDS:** high-performance, mixed-phase ZnMgO, photodetectors, low dark current, high responsivity, heterojunction interfaces



## INTRODUCTION

ZnO has caught the world's attention in the field of ultraviolet (UV) optoelectronic devices including UV photodetectors and UV light-emitters because of its excellent material properties: large excitonic binding energy (60 meV), high exciton density, large electron saturation velocity, low defect density, easy fabrication, high radiation hardness, and environmental friendly.<sup>1–5</sup> ZnMgO (ZMO), which is formed by alloying MgO with ZnO, shows the same material advantages as pure ZnO, and its band gap can be tuned continually from 3.37 eV (ZnO) to 7.8 eV (MgO), which covers UVA (320–400 nm), UVB (280–320 nm), and UVC (200–280 nm) regions.<sup>6–11</sup> Thus, it opens the possibility of developing the wavelength-tunable UV (200–400 nm) optoelectronic devices based on ZMO alloys. In particular, owing to their low operating voltage, intrinsic visible blind, and all solid state, ZMO-based photodetectors are recognized as one of the most potential alternative to the conventional photomultiplier tubes and Si-based UV photodetectors, which have huge applications in ozone-layer monitoring, ultrahigh temperature flame detection, convert space-to-space communication and missile warning systems, etc.<sup>12–20</sup> Till now, photodetectors based on cubic rock-salt ZMO (c-ZMO), wurtzite ZMO (w-ZMO), and mixed-phase

ZMO (m-ZMO) have been widely studied. According to the previous reports, w-ZMO photodetectors usually have a large responsivity, but their dark current is also relatively high.<sup>7–10,21,22</sup> In contrast, c-ZMO photodetectors possess low dark current and low responsivity.<sup>11–13,23,24</sup> Obviously, the photodetectors based on w-ZMO and c-ZMO cannot meet the performance standards for an ideal photodetector: both low dark current and high responsivity. In addition, without buffer layers and/or a slow growth rate, it is difficult to grow pure w- and c-ZMO with the band gap between 280 and 300 nm due to the phase segregation.<sup>9–11,25</sup> As for m-ZMO, it has long been regarded as a byproduct of the growth of high quality single phase ZMO and rarely been investigated, but recent results indicated that the photodetectors based on m-ZMO usually have large responsivity.<sup>9,14–18</sup> Unfortunately, two clear and uncontrollable response bands (one is in UVC region, and the other is in UVA or UVB region) and relatively large dark current in reported mixed-phase devices limit their applications.<sup>9,15–17</sup> By analyzing the previous results, it can be found

Received: May 28, 2015

Accepted: September 1, 2015

Published: September 1, 2015

that the above-mentioned problems in m-ZMO should be strongly associated with their growth substrates.<sup>9,15–17</sup> More recently, using *a*-face sapphire (*a*-Al<sub>2</sub>O<sub>3</sub>) as a substrate, our group has successfully demonstrated high-performance m-ZMO UV photodetector with a single cutoff wavelength in UVC region.<sup>18</sup> Interestingly, this m-ZMO photodetector exhibited a high responsivity and a low dark current. Thus, the m-ZMO fabricated on *a*-Al<sub>2</sub>O<sub>3</sub> seems more suitable for high-performance UV photodetection, compared to pure *w*- and *c*-ZMO. However, the growth mechanism of m-ZMO with single absorption edge and the origin of excellent performance of their UV photodetectors are still not very clear. In addition, the composition extension of m-ZMO with single absorption edge is urgently needed from a practical point of view.

In this article, m-ZMO films on *a*-Al<sub>2</sub>O<sub>3</sub> with tunable single optical absorption edge were successfully achieved by plasma-assisted molecular beam epitaxy (P-MBE), and the interactions among *c*-ZMO, *w*-ZMO, and the substrate for the m-ZMO have been analyzed. The small lattice mismatch of both *c*-ZMO (111)/*a*-Al<sub>2</sub>O<sub>3</sub> and *w*-ZMO (0002)/*a*-Al<sub>2</sub>O<sub>3</sub> should be the key reason for the single optical absorption edge in our m-ZMO. Moreover, by controlling the source temperature of Zn and Mg, the optical absorption edge of m-ZMO can be easily controlled and tuned. On the basis of these m-ZMO films, the interdigitated metal–semiconductor–metal (MSM) photodetectors were demonstrated with different  $-3$  dB cutoff wavelengths from 335 to 275 nm. In particular, for the devices with the cutoff wavelength at 330 nm (m-Z<sub>0.67</sub>M<sub>0.33</sub>O), 320 nm (m-Z<sub>0.59</sub>M<sub>0.41</sub>O), and 280 nm (m-Z<sub>0.39</sub>M<sub>0.61</sub>O), their dark current is around 78, 11, and 4 pA at 40 V, respectively. Meanwhile, the peak responsivity is 434 A/W (m-Z<sub>0.67</sub>M<sub>0.33</sub>O), 89.8 A/W (m-Z<sub>0.59</sub>M<sub>0.41</sub>O), and 3.7 A/W (m-Z<sub>0.39</sub>M<sub>0.61</sub>O). As indicated in resonant Raman spectra, the grain boundaries between *c*-ZMO and *w*-ZMO should be mainly responsible for the high performance of m-ZMO photodetectors. Our findings in this work show a promising prospect of m-ZMO photodetectors to be applied in UV photodetection.

## EXPERIMENTAL SECTION

m-ZMO epitaxial films were fabricated on *a*-Al<sub>2</sub>O<sub>3</sub> substrates by P-MBE deposition system employing solid Zn (6N) and Mg (5N) sources and atomic oxygen from O<sub>2</sub> (5N) activated in a radio frequency plasma cell. During deposition, the chamber pressure was maintained at 10<sup>-3</sup> Pa and the substrate temperature was 450 °C. The radio frequency power was fixed at 300 W with O<sub>2</sub> flow rate of 1.1 sccm. To fabricate m-ZMO thin films with different single absorption edges, we kept the Zn source temperature at 210 °C and tuned the Mg source temperature from 302 to 320 °C. All the samples were characterized using scanning electron microscope (SEM) (HITACHI S-4800), energy dispersive X-ray spectrometer (EDS) (GENESIS 2000 XMS60S), Bruker D8GADDS X-ray diffractometer (XRD) using Cu K $\alpha$  radiation ( $\lambda = 0.154$  nm) with an area detector, resonant Raman scattering spectra using He–Cd laser line of 325 nm as an excitation source, and UV-3101PC scanning spectrophotometer. Au interdigital electrodes (50 nm thick) were prepared on all samples through photolithography and a wet etching procedure to form MSM photodetectors. The current–voltage (*I*–*V*) properties (in dark and under illumination) and spectral responses of the photodetectors were measured by using a semiconductor device analyzer (Agilent B1500A) and a 200 W UV-enhanced Xe lamp with a monochromator, respectively. The transient response spectra of photodetectors were recorded by using an oscilloscope (Tektronix DPO 5104 digital oscilloscope) and a Nd:YAG laser (266 nm).

## RESULTS AND DISCUSSION

The m-ZMO films with different compositions were fabricated by controlling the temperature of Mg and Zn sources, and all the samples were characterized by XRD, EDS, SEM, and so on. Figure 1a shows the typical cross-sectional SEM image of m-

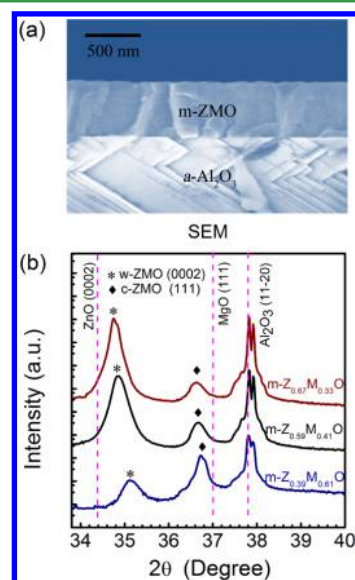


**Figure 1.** (a) Typical cross-sectional SEM image of m-ZMO. (b) XRD of m-Z<sub>0.67</sub>M<sub>0.33</sub>O, m-Z<sub>0.59</sub>M<sub>0.41</sub>O, and m-Z<sub>0.39</sub>M<sub>0.61</sub>O.

ZMO, indicating the thickness of the deposited films is around 500 nm. The composition of m-ZMO was evaluated by EDS, which can be found in the Supporting Information (see Figure S1). In order to analyze the structural properties, the  $2\theta$ – $\theta$  XRD measurement was carried out for three typical samples: m-Z<sub>0.67</sub>M<sub>0.33</sub>O, m-Z<sub>0.59</sub>M<sub>0.41</sub>O, and m-Z<sub>0.39</sub>M<sub>0.61</sub>O, as shown in Figure 1b. Besides the substrate diffraction peak, two peaks associated with m-ZMO can be clearly found in three samples. The peaks located at around 35° and 36° correspond to the diffraction of *w*-ZMO (0002) and *c*-ZMO (111), respectively. Obviously, with Mg content increasing, both (0002) and (111) peaks shift toward the big angle side because of the substitution of Zn atoms by Mg atoms as well as lattice stress effects.<sup>18</sup> Figure 2a presents the resonant Raman scattering spectra of m-Z<sub>0.67</sub>M<sub>0.33</sub>O, m-Z<sub>0.39</sub>M<sub>0.61</sub>O, ZnO, and *c*-Z<sub>0.3</sub>M<sub>0.7</sub>O. ZnO and *c*-Z<sub>0.3</sub>M<sub>0.7</sub>O are used as control samples, and their detailed properties can be found in Supporting Information (see Figures S2–S5). For each control sample, only one Raman peak can be observed ( $\sim 570$  cm<sup>-1</sup> for ZnO and  $\sim 643$  cm<sup>-1</sup> for *c*-Z<sub>0.3</sub>M<sub>0.7</sub>O), which corresponds to the first and second order longitude optical (LO) phonon modes, respectively.<sup>1,26</sup> In contrast, a broad band between 570 and 643 cm<sup>-1</sup> can be clearly obtained for both m-Z<sub>0.67</sub>M<sub>0.33</sub>O and m-Z<sub>0.39</sub>M<sub>0.61</sub>O instead of two distinct LO phonon modes of *w*-ZMO and *c*-ZMO. As is well-known, the broadening of LO phonon modes is usually induced by the effect of alloy fluctuation, defects, and grain boundaries.<sup>27–29</sup> Compared with the pure *c*- and *w*-ZMO, m-ZMO shows much more grain boundaries between *w*- and *c*-ZMO. Thus, these grain boundaries should be the main reason for the broad Raman band of m-ZMO as shown in Figure 2a. In addition, the alloy fluctuation and intrinsic defects in m-ZMO also cannot be excluded.

Figure 2b shows the transmission spectra of m-Z<sub>0.67</sub>M<sub>0.33</sub>O, m-Z<sub>0.59</sub>M<sub>0.41</sub>O, and m-Z<sub>0.39</sub>M<sub>0.61</sub>O. The average transmittance

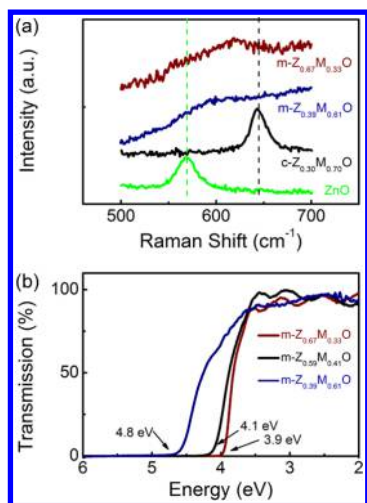


**Figure 2.** (a) Resonant Raman scattering and (b) transmission spectra of  $m\text{-Z}_{0.67}\text{M}_{0.33}\text{O}$ ,  $m\text{-Z}_{0.59}\text{M}_{0.41}\text{O}$ , and  $m\text{-Z}_{0.39}\text{M}_{0.61}\text{O}$  at room temperature. Resonant Raman scattering spectra of ZnO and  $c\text{-Z}_{0.3}\text{M}_{0.7}\text{O}$  are also displayed in (a) as references.

of all three samples in the visible region was more than 85%. Although  $w\text{-ZMO}$  and  $c\text{-ZMO}$  coexist, the single optical transmission edge at  $\sim 3.9$ ,  $\sim 4.1$ , and  $\sim 4.8$  eV can be clearly observed for  $m\text{-Z}_{0.67}\text{M}_{0.33}\text{O}$ ,  $m\text{-Z}_{0.59}\text{M}_{0.41}\text{O}$ , and  $m\text{-Z}_{0.39}\text{M}_{0.61}\text{O}$ , respectively. This result is much different from that obtained in  $m\text{-ZMO}$  on other substrates (such as Si, quartz,  $c\text{-Al}_2\text{O}_3$ , and MgO), which usually possess two uncontrollable optical absorption edges (see Figure S6 in Supporting Information).<sup>16,17,30–33</sup> Notably, differing from that of the pure cubic or hexagonal ZMO, the single absorption/transmission edge of  $m\text{-ZMO}$  just means that the band gap of the cubic and hexagonal phases in  $m\text{-ZMO}$  is similar but not exactly the same. And this can be confirmed by the relatively smooth transmission edge, especially for  $m\text{-Z}_{0.39}\text{M}_{0.61}\text{O}$ . The dependence of  $m\text{-ZMO}$  optical transmission property on substrates is associated with the difference in the nucleation and growth process of  $m\text{-ZMO}$  induced by the effect of lattice mismatch between  $c\text{-/}w\text{-ZMO}$  and substrate. In the previous reports, most  $m\text{-ZMO}$  films were fabricated on Si, quartz,  $c\text{-Al}_2\text{O}_3$ , and MgO. These substrates have relatively low lattice mismatch with either  $c\text{-ZMO}$  only or  $w\text{-ZMO}$  only (or have large lattice mismatch with both  $c\text{-ZMO}$  and  $w\text{-ZMO}$ ).<sup>1,34–36</sup> Thus, during the deposition of  $m\text{-ZMO}$ , single-phase ZMO (either  $w\text{-ZMO}$  or  $c\text{-ZMO}$ ) is usually deposited on the substrate at the initial growth stage. Subsequently,  $w\text{-ZMO}$  ( $c\text{-ZMO}$ ) would precipitate from oversaturated  $c\text{-ZMO}$  ( $w\text{-ZMO}$ ) with the large composition difference between them, and this process is difficult to be controlled.<sup>33,37</sup> Thus, the traditional  $m\text{-ZMO}$

fabricated on Si, quartz,  $c\text{-Al}_2\text{O}_3$ , and MgO usually have two obviously distinguished and uncontrollable optical absorption edges.

As for the growth of  $m\text{-ZMO}$  on  $a\text{-Al}_2\text{O}_3$ , its process is much different from that on other substrates because of the small lattice mismatch of both  $c\text{-ZMO}/a\text{-Al}_2\text{O}_3$  and  $w\text{-ZMO}/a\text{-Al}_2\text{O}_3$ .<sup>1,36</sup> Figure 3 is the schematic diagram of the atom arrangement and the relative orientation of ZnO (0002), MgO (111), and  $a\text{-Al}_2\text{O}_3$  (11 $\bar{2}$ 0) surfaces. For ZnO grown on  $a\text{-Al}_2\text{O}_3$ , the orientation relationship along the direction normal to the surface is ZnO (0001)|| $a\text{-Al}_2\text{O}_3$  (11 $\bar{2}$ 0) and the in-plane orientational relationships are ZnO [11 $\bar{2}$ 0]|| $a\text{-Al}_2\text{O}_3$  [0001] and ZnO [ $\bar{1}$ 100]|| $a\text{-Al}_2\text{O}_3$  [ $\bar{1}$ 100]. In case of MgO grown on  $a\text{-Al}_2\text{O}_3$ , the orientation relationship along the direction normal to the surface is MgO (111)|| $a\text{-Al}_2\text{O}_3$  (11 $\bar{2}$ 0) and the in-plane orientational relationships are MgO [ $\bar{1}$ 12]|| $a\text{-Al}_2\text{O}_3$  [0001] and MgO [ $\bar{1}$ 10]|| $a\text{-Al}_2\text{O}_3$  [ $\bar{1}$ 100]. Thus, the lattice mismatch of ZnO with  $a\text{-Al}_2\text{O}_3$  is  $-0.03\%$  along the [0001] direction and is  $-2.4\%$  along the [ $\bar{1}$ 100] direction, while the lattice mismatch of MgO with  $a\text{-Al}_2\text{O}_3$  is  $0.7\%$  along the [0001] direction and is  $-1.2\%$  along the [ $\bar{1}$ 100] direction. The detailed calculation process can be found in the Supporting Information. As is well-known, lattice-matched substrate or buffer layers can greatly improve the solubility limit and extend the composition and band gap of ZMO, and the controllable growth of  $w\text{-ZMO}$  or  $c\text{-ZMO}$  with widely tunable band gap can be realized.<sup>9–11,25</sup> On the basis of the above calculation, it can be found that  $a\text{-Al}_2\text{O}_3$  has a small mismatch with both ZnO and MgO, and thus, the growth of both  $w\text{-ZnO}$  and  $c\text{-ZMO}$  can be controlled. The detailed possible growth mechanism of  $m\text{-ZMO}$  with single absorption edge was proposed as the following: at the fixed temperature of Zn and Mg source,  $w\text{-ZMO}$  and  $c\text{-ZMO}$  with close bandgap randomly nucleate on substrate at the initial period of growth, instead of preferred growth of ZMO with the special kind of crystal structure, and gradually grow up until the end of growth. With increasing of the temperature of Mg source, the Mg/Zn ratio and the bandgap of  $w\text{-ZMO}$  and  $c\text{-ZMO}$  increase, and the single absorption edge of thin films is thus adjusted.

Accordingly,  $m\text{-ZMO}$  UV photodetectors with tunable cutoff wavelengths can be easily realized based on the above  $m\text{-ZMO}$  thin films on  $a\text{-Al}_2\text{O}_3$ . Figure 4a is the schematic diagram of the MSM photodetector (not to scale). Twelve pairs of Au interdigital fingers ( $5\ \mu\text{m}$  width,  $5\ \mu\text{m}$  gap, and  $500\ \mu\text{m}$  length) on  $m\text{-ZMO}$  were achieved through photolithography and a wet etching procedure. As shown in Figure 4b, the  $I\text{-}V$  characteristics of the  $m\text{-Z}_{0.67}\text{M}_{0.33}\text{O}$ ,  $m\text{-Z}_{0.59}\text{M}_{0.41}\text{O}$ , and  $m\text{-Z}_{0.39}\text{M}_{0.61}\text{O}$  photodetectors were measured in a dark condition and under UV illumination. At 40 V,  $m\text{-Z}_{0.67}\text{M}_{0.33}\text{O}$ ,  $m\text{-Z}_{0.59}\text{M}_{0.41}\text{O}$ , and  $m\text{-Z}_{0.39}\text{M}_{0.61}\text{O}$  devices exhibit the extremely low dark current of

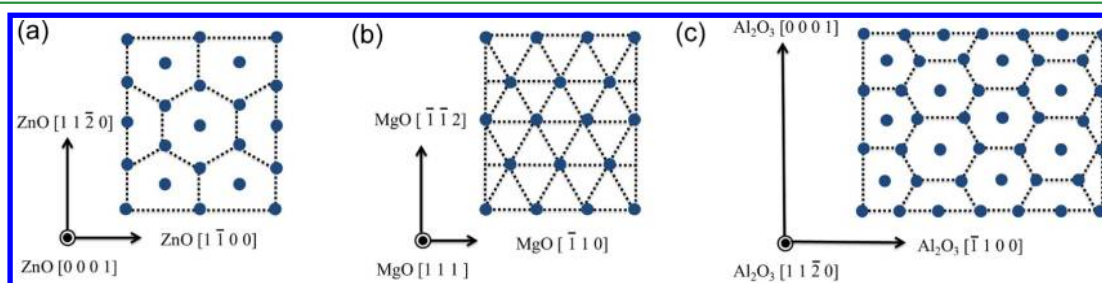


**Figure 3.** (a) ZnO (0002), (b) MgO (111), and (c)  $a\text{-Al}_2\text{O}_3$  (11 $\bar{2}$ 0) surfaces atom arrangements and relative orientations.

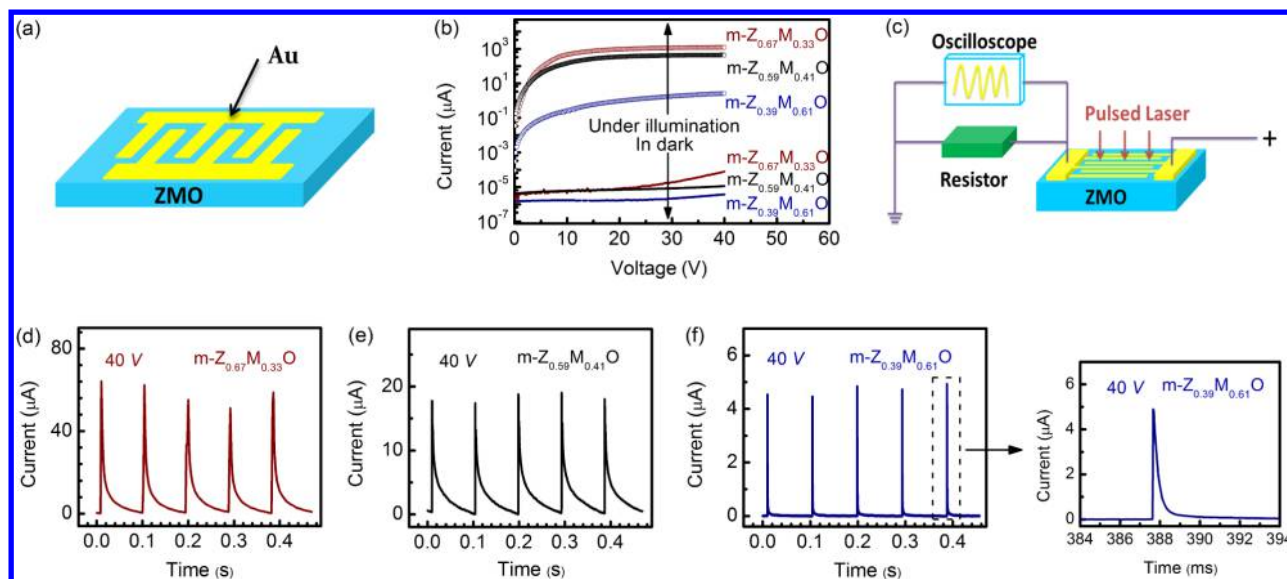


**Figure 4.** (a) Schematic diagram of MSM photodetector (not to scale). (b)  $I$ - $V$  characteristics of the  $m\text{-Z}_{0.67}\text{M}_{0.33}\text{O}$ ,  $m\text{-Z}_{0.59}\text{M}_{0.41}\text{O}$ , and  $m\text{-Z}_{0.39}\text{M}_{0.61}\text{O}$  photodetectors in a dark condition and under UV illumination. (c) Schematic diagram of experimental setup for the measurement of response time. Transient response of  $m\text{-ZMO}$  photodetector was analyzed by using a pulsed Nd:YAG laser with a wavelength of 266 nm (the laser pulse width was 10 ns, and the frequency was 10 Hz) and a digital oscilloscope. (d), (e), and (f) are the transient response of  $m\text{-Z}_{0.67}\text{M}_{0.33}\text{O}$ ,  $m\text{-Z}_{0.59}\text{M}_{0.41}\text{O}$ , and  $m\text{-Z}_{0.39}\text{M}_{0.61}\text{O}$  photodetectors at 40 V, respectively. The right of (f) is the response of  $m\text{-Z}_{0.39}\text{M}_{0.61}\text{O}$  photodetector in a single cycle.

only 78, 11, and 4 pA, respectively. Under UV illumination, the current of the  $m\text{-Z}_{0.67}\text{M}_{0.33}\text{O}$  device ( $\lambda = 320$  nm, power density =  $1 \text{ mW/cm}^2$ ),  $m\text{-Z}_{0.59}\text{M}_{0.41}\text{O}$  device ( $\lambda = 306$  nm, power density =  $0.8 \text{ mW/cm}^2$ ), and  $m\text{-Z}_{0.39}\text{M}_{0.61}\text{O}$  device ( $\lambda = 255$  nm, power density =  $0.6 \text{ mW/cm}^2$ ) is 456, 145, and 2.66  $\mu\text{A}$ , respectively. The photo-to-dark current ratio is more than 5 orders of magnitude. For the application of photodetector in the optical switching devices or optical communication systems, response speed is an important figure of merit. Figure 4c is the schematic diagram of the experimental setup for the measurement of response time. The transient response of  $m\text{-ZMO}$  photodetector was analyzed by using a pulsed Nd:YAG laser with a wavelength of 266 nm (the laser pulse width was 10 ns, and the frequency was 10 Hz) and a digital oscilloscope. As shown in Figure 4d–f, the photoresponse of  $m\text{-ZMO}$  was very fast, highly stable, and reproducible. The 90–10% decay time can be estimated to be  $\sim 37$ ,  $\sim 30$ , and  $\sim 0.7$  ms for  $m\text{-Z}_{0.67}\text{M}_{0.33}\text{O}$ ,  $m\text{-Z}_{0.59}\text{M}_{0.41}\text{O}$ , and  $m\text{-Z}_{0.39}\text{M}_{0.61}\text{O}$ , respectively.

Figure 5a is the photoresponse spectra of  $m\text{-ZMO}$  photodetectors at 10 V bias in logarithmic scale (200 W UV-enhanced Xe lamp with a monochromator as light source). The peak responsivity is  $\sim 32 \text{ A/W}$  (320 nm),  $\sim 1.9 \text{ A/W}$  (306 nm), and  $\sim 0.2 \text{ A/W}$  (255 nm) for  $m\text{-Z}_{0.67}\text{M}_{0.33}\text{O}$ ,  $m\text{-Z}_{0.59}\text{M}_{0.41}\text{O}$ , and  $m\text{-Z}_{0.39}\text{M}_{0.61}\text{O}$ , respectively. The  $-3$  dB cutoff edge is around 330 nm ( $m\text{-Z}_{0.67}\text{M}_{0.33}\text{O}$ ), 320 nm ( $m\text{-Z}_{0.59}\text{M}_{0.41}\text{O}$ ), and 280 nm ( $m\text{-Z}_{0.39}\text{M}_{0.61}\text{O}$ ), which is in good accordance with the optical transmission edges in Figure 2b. As shown in Figure 5a, the UV–visual rejection ratio, defined as the ratio between the peak responsivity and responsivity at 400 nm, can reach as large as  $10^5$  for  $m\text{-Z}_{0.67}\text{M}_{0.33}\text{O}$  and  $m\text{-Z}_{0.59}\text{M}_{0.41}\text{O}$  devices. Notably, there is a very weak shoulder around 320 nm in spectral response of the  $m\text{-Z}_{0.39}\text{M}_{0.61}\text{O}$  photodetector. This result is in good agreement with the transmission spectrum of  $m\text{-Z}_{0.39}\text{M}_{0.61}\text{O}$  in Figure 2b, in which a weak absorption around 320 nm can be clearly observed because of the little difference of the band gap between  $c$ - and  $w\text{-ZMO}$ . Figure 5b shows the peak responsivity as a function of bias voltage. A liner relationship can be

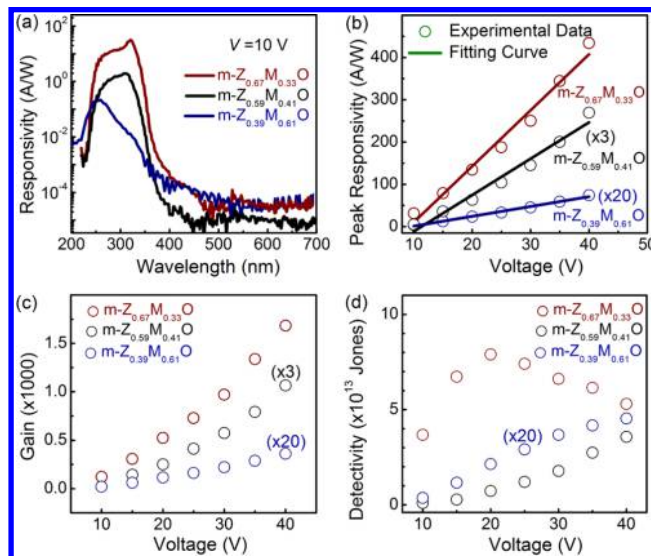


**Figure 5.** (a) Spectral response of the  $m\text{-Z}_{0.67}\text{M}_{0.33}\text{O}$ ,  $m\text{-Z}_{0.59}\text{M}_{0.41}\text{O}$ , and  $m\text{-Z}_{0.39}\text{M}_{0.61}\text{O}$  photodetectors at 10 V bias in logarithmic scale. (b) Peak responsivity, (c) gain, and (d) detectivity of the  $m\text{-Z}_{0.67}\text{M}_{0.33}\text{O}$ ,  $m\text{-Z}_{0.59}\text{M}_{0.41}\text{O}$ , and  $m\text{-Z}_{0.39}\text{M}_{0.61}\text{O}$  photodetectors as a function of bias voltage.

observed between 10 and 40 V for all devices, indicating no carrier mobility saturation or sweep-out effect up to 40 V.<sup>38</sup> At 40 V, the peak responsivity of  $m\text{-Z}_{0.67}\text{M}_{0.33}\text{O}$ ,  $m\text{-Z}_{0.59}\text{M}_{0.41}\text{O}$ , and  $m\text{-Z}_{0.39}\text{M}_{0.61}\text{O}$  photodetectors can reach as high as 434, 89.8, and 3.7 A/W, respectively. According to the previous reports, the responsivity ( $R$ ) of photodetectors can be expressed as the following function:<sup>38</sup>

$$R = \frac{q\lambda\eta G}{hc} \quad (1)$$

where  $q$  is the elementary charge,  $\lambda$  is the wavelength,  $\eta$  is the quantum efficiency,  $G$  is internal gain,  $h$  is Planck's constant,

and  $c$  is the light velocity. Thus, assuming the quantum efficiency is 100%, the internal gain of the devices can be calculated from eq 1 with different applied voltages as shown in Figure 5c. At 40 V, the internal gain of m-Z<sub>0.67</sub>M<sub>0.33</sub>O, m-Z<sub>0.59</sub>M<sub>0.41</sub>O, and m-Z<sub>0.39</sub>M<sub>0.61</sub>O photodetectors is about 1684, 356, and 18, respectively. In addition to responsivity, detectivity is another important figure of merit reflecting the photodetector sensitivity to incident light. Considering the major sources of noise should be the thermal noise and the shot noise from dark current in our devices, the detectivity ( $D^*$ ) can be quantified by the following equation:<sup>38–40</sup>

$$D^* = \frac{A^{1/2}R}{(4k_0T/R_{\text{dark}} + 2qI_{\text{dark}})^{1/2}} \quad (2)$$

where  $A$  is the active area,  $R$  is the responsivity,  $k_0$  is the Boltzmann constant,  $T$  is the temperature,  $R_{\text{dark}}$  is the equivalent resistance obtained from the slope of the dark current  $I$ – $V$  curve at the bias point,  $q$  is the elementary charge, and  $I_{\text{dark}}$  is the dark current at the bias point. The detectivity as a function of bias voltage is indicated in Figure 5d. The maximum detectivity of m-Z<sub>0.67</sub>M<sub>0.33</sub>O, m-Z<sub>0.59</sub>M<sub>0.41</sub>O, and m-Z<sub>0.39</sub>M<sub>0.61</sub>O photodetectors is  $7.9 \times 10^{13}$ ,  $3.5 \times 10^{13}$ , and  $2.26 \times 10^{12}$  Jones, respectively. The large detectivity is associated with low dark current and high responsivity, the origin of which will be discussed in the following part.

Considering the mixed-phase nature of our ZMO films, the operation mechanism of the MSM structured photodetector is proposed and schematically presented in Figure 6. As shown in Figure 6a, c- and w-ZMO are uniformly and dispersedly grown on the surface of  $\alpha$ -Al<sub>2</sub>O<sub>3</sub> substrate at the same time. The c-ZMO usually has high inherent resistance, which can be mainly

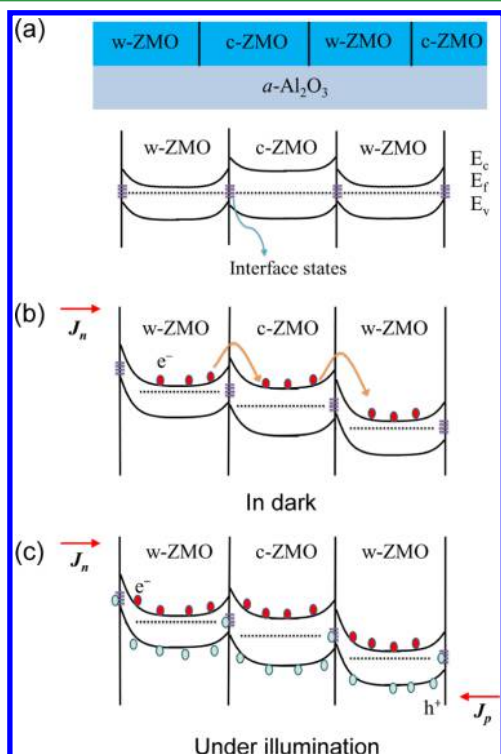


**Figure 6.** Energy band diagram and carrier transport process of m-ZMO photodetector at different conditions: (a) at thermal equilibrium, (b) under bias in dark, and (c) under bias with UV illumination.

responsible for the low dark current of our m-ZMO photodetectors.<sup>11–13,24</sup> Apart from that, the low dark current can be also caused by large amounts of heterojunctions between w-ZMO and c-ZMO. According to the previous reports, the electrons could be trapped at interfaces between c-ZMO and w-ZMO, inducing the potential barriers as shown in the bottom of Figure 6a.<sup>18,41–43</sup> When the bias voltage is applied on the m-ZMO photodetector, these potential barriers impede the flow of electrons in m-ZMO in dark (see Figure 6b), which is partly responsible for the small dark current of the devices. As for the m-ZMO thin films fabricated on the other substrates, the growth process of one phase precipitating from another oversaturated phase determines that the distribution of c- and w-ZMO is very uneven.<sup>33,37</sup> Thus, the carriers can easily flow through the low-resistance w-ZMO, resulting in a relatively large dark current (see Figure S7). When we turn on the UV light (see Figure 6c), the electron–hole pairs are excited and the photogenerated holes are driven by electric field and trapped at the c-/w-ZMO interfaces, prolonging their lifetime. As is well-known, the internal photoconductive gain  $G$  can be expressed as the following equation:  $G = \tau/t$  (where  $\tau$  is the lifetime of photogenerated holes and  $t$  is the transit time of electrons); thus, the large photoresponsivity (internal gain) in our m-ZMO devices should be associated with the prolonged lifetime of photogenerated holes.<sup>11</sup> Besides the interface defect between c- and w-ZMO, deep defects (such as zinc vacancies or oxygen interstitials located above valence band) in ZMO should also partly contribute to the long lifetime of holes and the photoconductive gain.<sup>1,10,11,21,44–46</sup>

Table 1 summarizes the representative reported w-ZMO, c-ZMO, and m-ZMO photodetectors, whose cutoff wavelengths are similar to our devices. Compared with the single-phase ZMO devices, although the decay speed is a little slow, m-Z<sub>0.67</sub>M<sub>0.33</sub>O, m-Z<sub>0.59</sub>M<sub>0.41</sub>O, and m-Z<sub>0.39</sub>M<sub>0.61</sub>O devices possess low dark current, high responsivity, and large rejection ratio at the same time. As for the relatively slow decay of m-ZMO devices, the interface defects at heterojunction boundaries should be the main reason because they can act as the traps of holes, prolonging the lifetime of minor carriers. In contrast, owing to the absence of these heterojunction traps, the decay speed of single-phase ZMO devices is much quicker than that of m-ZMO ones. In comparison to the most m-ZMO devices fabricated on other substrates, our devices not only have the single cutoff wavelength but also show lower dark current, faster decay time, higher rejection ratio, and comparable responsivity. Notably, m-Z<sub>0.66</sub>M<sub>0.34</sub>O photodetector reported by W. Yang et al. possessed higher responsivity and faster decay time.<sup>14</sup> In fact, from their XRD results, the ultraweak diffraction peak of c-ZMO indicated that the content of c-ZMO is very little, and thus, it contributes little to the overall characteristics of m-Z<sub>0.66</sub>M<sub>0.34</sub>O. In other words, the m-Z<sub>0.66</sub>M<sub>0.34</sub>O in ref 14 is more like the pure w-ZMO with high responsivity and large dark current. Additionally, our m-ZMO devices possess large detectivity, which is a requisite to achieve a high signal-to-noise ratio for photodetectors in weak signal detection, especially. In a word, our devices possess good comprehensive performance than the other ZMO photodetectors, such as low dark current, high responsivity, relatively fast response speed, high rejection ratio, and large detectivity.

## CONCLUSIONS

m-ZMO thin films with single and tunable optical absorption edges were successfully grown on  $\alpha$ -Al<sub>2</sub>O<sub>3</sub> by P-MBE, which is

**Table 1.** Dark Current, Peak Responsivity, Cutoff Wavelength, Rejection Ratio, and Decay Time of Photodetectors Based on w-ZMO, c-ZMO, and m-ZMO

	substrate	dark current (pA)	peak responsivity (A/W)	cutoff wavelength (nm)	rejection ratio	decay time (90–10%) (ms)	ref
w-Z <sub>0.66</sub> M <sub>0.34</sub> O	Si	7.67 × 10 <sup>3</sup> (5 V)	34.02 (5 V)	~330	~5	120	7
w-Z <sub>0.6</sub> M <sub>0.4</sub> O	quartz	4.2 × 10 <sup>4</sup> (3 V)	1 (3 V)	~330	~10	3.9 × 10 <sup>-5</sup>	8
w-Z <sub>0.54</sub> M <sub>0.46</sub> O	c-Al <sub>2</sub> O <sub>3</sub>	2.7 × 10 <sup>6</sup> (5 V)	201 (5 V)	~280	140		9
w-Z <sub>0.54</sub> M <sub>0.46</sub> O	quartz		3.4 (10 V)	~280	10 <sup>3</sup>	0.462	10
c-Z <sub>0.51</sub> M <sub>0.49</sub> O	a-Al <sub>2</sub> O <sub>3</sub>	3 (10 V)	5.188 (10 V)	~320	10 <sup>3</sup>	0.024	11
c-Z <sub>0.46</sub> M <sub>0.54</sub> O	c-Al <sub>2</sub> O <sub>3</sub>	0.45 (10 V)	0.396 (10 V)	265	10		12
c-Z <sub>0.48</sub> M <sub>0.52</sub> O	MgO	16 (15 V)	0.129 (15 V)	253	10 <sup>4</sup>	1 × 10 <sup>-3</sup>	13
m-Z <sub>0.66</sub> M <sub>0.34</sub> O	c-Al <sub>2</sub> O <sub>3</sub>	4 × 10 <sup>4</sup> (5 V)	1200 (5 V)	317	10 <sup>4</sup>	1.4 × 10 <sup>-3</sup>	14
m-ZMO	MgO		462 (1 V)	~275, ~370		2.5 × 10 <sup>4</sup>	9
m-ZMO	MgO		3 (1 V)	~280, ~350		3 × 10 <sup>4</sup>	15
m-ZMO	MgO		60 (1 V)	~275, ~350		2 × 10 <sup>4</sup>	16
m-ZMO	Si	1 × 10 <sup>3</sup> (-1.5 V)	0.032 (-1.5 V)	~280, ~400			17
m-Z <sub>0.38</sub> M <sub>0.62</sub> O	a-Al <sub>2</sub> O <sub>3</sub>	2 (10 V)	1.664 (10 V)	275	10 <sup>3</sup>	~1 × 10 <sup>3</sup>	18
m-Z <sub>0.67</sub> M <sub>0.33</sub> O	a-Al <sub>2</sub> O <sub>3</sub>	4 (10 V)	32 (10 V)	330	10 <sup>5</sup>	37	this work
m-Z <sub>0.59</sub> M <sub>0.41</sub> O	a-Al <sub>2</sub> O <sub>3</sub>	6 (10 V)	1.9 (10 V)	320	10 <sup>5</sup>	30	this work
m-Z <sub>0.39</sub> M <sub>0.61</sub> O	a-Al <sub>2</sub> O <sub>3</sub>	2 (10 V)	0.2 (10 V)	280	10 <sup>3</sup>	0.7	this work

associated with the small lattice mismatch of both ZnO and MgO with a-Al<sub>2</sub>O<sub>3</sub>. On the basis of these films, m-ZMO MSM photodetectors were realized with the single cutoff wavelength tuning from 335 to 275 nm. At 40 V, the dark current of m-Z<sub>0.67</sub>M<sub>0.33</sub>O, m-Z<sub>0.59</sub>M<sub>0.41</sub>O, and m-Z<sub>0.39</sub>M<sub>0.61</sub>O devices is only 78, 11, and 4 pA, respectively. Meanwhile, the responsivity can reach as large as 434 A/W (m-Z<sub>0.67</sub>M<sub>0.33</sub>O), 89.8 A/W (m-Z<sub>0.59</sub>M<sub>0.41</sub>O), and 3.7 A/W (m-Z<sub>0.39</sub>M<sub>0.61</sub>O). The excellent photoelectric characteristics of m-ZMO MSM photodetectors are associated with the heterojunction interfaces between w-ZMO and c-ZMO. What is more, the response speed of m-Z<sub>0.67</sub>M<sub>0.33</sub>O, m-Z<sub>0.59</sub>M<sub>0.41</sub>O, and m-Z<sub>0.39</sub>M<sub>0.61</sub>O is around 37, 30, and 0.7 ms, respectively. Compared with other ZMO photodetectors with similar cutoff wavelengths, our devices have more excellent comprehensive performance, including low dark current, high responsivity, relatively fast response speed, and large detectivity. Owing to the easy fabrication process and excellent performance, the m-ZMO-based UV photodetectors should have huge potential applications in many fields.

## ■ ASSOCIATED CONTENT

### Supporting Information

The Supporting Information is available free of charge on the ACS Publications website at DOI: 10.1021/acsami.Sb04671.

- (a) EDS results of m-Z<sub>0.67</sub>M<sub>0.33</sub>O, m-Z<sub>0.59</sub>M<sub>0.41</sub>O, and m-Z<sub>0.39</sub>M<sub>0.61</sub>O; (b) characteristics of ZnO and c-Z<sub>0.30</sub>M<sub>0.70</sub>O; (c) calculation process of lattice mismatch between ZnO or MgO with a-Al<sub>2</sub>O<sub>3</sub>; (d) characteristics of m-ZMO on c-Al<sub>2</sub>O<sub>3</sub> (PDF)

## ■ AUTHOR INFORMATION

### Corresponding Authors

\*K.-W.L.: e-mail, liukw@ciomp.ac.cn.

\*D.-Z.S.: e-mail, shendz@ciomp.ac.cn.

### Notes

The authors declare no competing financial interest.

## ■ ACKNOWLEDGMENTS

This work is supported by the National Basic Research Program of China (973 Program) (Grants 2011CB302002, 2011CB302006), the National Natural Science Foundation of China (Grants 61475153, 10974197, 11174273, 11104265,

11134009, 61177040), and the 100 Talents Program of the Chinese Academy of Sciences, Jilin Province Human Resources and Social Security Hall (Grant RL201301).

## ■ REFERENCES

- Özgür, Ü.; Alivov, Y. I.; Liu, C.; Teke, A.; Reshchikov, M. A.; Doğan, S.; Avrutin, V.; Cho, S.-J.; Morkoç, H. A Comprehensive Review of ZnO Materials and Devices. *J. Appl. Phys.* **2005**, *98*, 041301.
- Jiao, S. J.; Lu, Y. M.; Shen, D. Z.; Zhang, Z. Z.; Li, B. H.; Zhang, J. Y.; Yao, B.; Liu, Y. C.; Fan, X. W. Ultraviolet Electroluminescence of ZnO Based Heterojunction Light Emitting Diode. *Phys. Status Solidi C* **2006**, *3*, 972–975.
- Albrecht, J. D.; Ruden, P. P.; Limpijumngong, S.; Lambrecht, W. R. L.; Brennan, K. F. High Field Electron Transport Properties of Bulk ZnO. *J. Appl. Phys.* **1999**, *86*, 6864–6867.
- Liu, K.; Sakurai, M.; Aono, M. ZnO-Based Ultraviolet Photodetectors. *Sensors* **2010**, *10*, 8604–8634.
- Lorenz, K.; Peres, M.; Franco, N.; Marques, J. G.; Miranda, S. M. C.; Magalhães, S.; Monteiro, T.; Wesch, W.; Alves, E.; Wendler, E. Radiation Damage Formation and Annealing in GaN and ZnO. *Oxide-Based Materials and Devices II*, Proceedings of SPIE 7940, San Francisco, CA, U.S., 2011; SPIE: Bellingham, WA, 2011; 79400O, DOI: 10.1117/12.879402.
- Zhang, Z.; von Wenckstern, H.; Grundmann, M. Energy-Selective Multichannel Ultraviolet Photodiodes Based on (Mg,Zn)O. *Appl. Phys. Lett.* **2013**, *103*, 171111.
- Li, G.; Zhang, J.; Liu, Y.; Zhang, K. Solar-Blind Photodetectors Based on Polycrystalline MgZnO Thin Films. *Opt. Eng.* **2011**, *50*, 113801.
- Jiang, D. Y.; Zhang, J. Y.; Liu, K. W.; Zhao, Y. M.; Cong, C. X.; Lu, Y. M.; Yao, B.; Zhang, Z. Z.; Shen, D. Z. A High-Speed Photoconductive UV Detector Based on an Mg<sub>0.4</sub>Zn<sub>0.6</sub>O Thin Film. *Semicond. Sci. Technol.* **2007**, *22*, 687–690.
- Schoenfeld, W. V.; Wei, M.; Boutwell, R. C.; Liu, H. High Response Solar-Blind MgZnO Photodetectors Grown by Molecular Beam Epitaxy. *Oxide-Based Materials and Devices V*, Proceedings of SPIE 8987, San Francisco, CA, U.S. 2014; SPIE: Bellingham, WA, 2014; 89871P, DOI: 10.1117/12.2045555.
- Zheng, Q.; Huang, F.; Huang, J.; Hu, Q.; Chen, D.; Ding, K. High-Responsivity Solar-Blind Photodetector Based on Mg<sub>0.46</sub>Zn<sub>0.54</sub>O Thin Film. *IEEE Electron Device Lett.* **2012**, *33*, 1033–1035.
- Fan, M.-M.; Liu, K.-W.; Chen, X.; Zhang, Z.-Z.; Li, B.-H.; Zhao, H.-F.; Shen, D.-Z. Realization of Cubic ZnMgO Photodetectors for UVB Applications. *J. Mater. Chem. C* **2015**, *3*, 313–317.
- Wang, L. K.; Ju, Z. G.; Zhang, J. Y.; Zheng, J.; Shen, D. Z.; Yao, B.; Zhao, D. X.; Zhang, Z. Z.; Li, B. H.; Shan, C. X. Single-Crystalline

Cubic MgZnO Films and Their Application in Deep-Ultraviolet Optoelectronic Devices. *Appl. Phys. Lett.* **2009**, *95*, 131113.

(13) Han, S.; Zhang, Z.; Zhang, J.; Wang, L.; Zheng, J.; Zhao, H.; Zhang, Y.; Jiang, M.; Wang, S.; Zhao, D.; Shan, C.; Li, B.; Shen, D. Photoconductive Gain in Solar-Blind Ultraviolet Photodetector Based on Mg<sub>0.52</sub>Zn<sub>0.48</sub>O Thin Film. *Appl. Phys. Lett.* **2011**, *99*, 242105.

(14) Yang, W.; Vispute, R. D.; Choo-pun, S.; Sharma, R. P.; Venkatesan, T.; Shen, H. Ultraviolet Photoconductive Detector Based on Epitaxial Mg<sub>0.34</sub>Zn<sub>0.66</sub>O Thin Films. *Appl. Phys. Lett.* **2001**, *78*, 2787–2789.

(15) Boutwell, R. C.; Wei, M.; Schoenfeld, W. V. The Effect of Substrate Temperature and Source Flux on Cubic ZnMgO UV Sensors Grown by Plasma-Enhanced Molecular Beam Epitaxy. *Appl. Surf. Sci.* **2013**, *284*, 254–257.

(16) Boutwell, R. C.; Wei, M.; Schoenfeld, W. V. The Effect of Oxygen Flow Rate and Radio Frequency Plasma Power on Cubic ZnMgO Ultraviolet Sensors Grown by Plasma-Enhanced Molecular Beam Epitaxy. *Appl. Phys. Lett.* **2013**, *103*, 031114.

(17) Xie, X. H.; Zhang, Z. Z.; Shan, C. X.; Chen, H. Y.; Shen, D. Z. Dual-Color Ultraviolet Photodetector Based on Mixed-Phase-MgZnO/i-MgO/p-Si Double Heterojunction. *Appl. Phys. Lett.* **2012**, *101*, 081104.

(18) Fan, M. M.; Liu, K. W.; Zhang, Z. Z.; Li, B. H.; Chen, X.; Zhao, D. X.; Shan, C. X.; Shen, D. Z. High-Performance Solar-Blind Ultraviolet Photodetector Based on Mixed-Phase ZnMgO Thin Film. *Appl. Phys. Lett.* **2014**, *105*, 011117.

(19) Xie, T.; Liu, G.; Wen, B.; Ha, J. Y.; Nguyen, N. V.; Motayed, A.; Debnath, R. Tunable Ultraviolet Photoresponse in Solution-Processed p-n Junction Photodiodes Based on Transition-Metal Oxides. *ACS Appl. Mater. Interfaces* **2015**, *7*, 9660–9667.

(20) Monroy, E.; Omnès, F.; Calle, F. Wide-Bandgap Semiconductor Ultraviolet Photodetectors. *Semicond. Sci. Technol.* **2003**, *18*, R33.

(21) Tabares, G.; Hierro, A.; Ulloa, J. M.; Guzman, A.; Muñoz, E.; Nakamura, A.; Hayashi, T.; Temmyo, J. High Responsivity and Internal Gain Mechanisms in Au-ZnMgO Schottky Photodiodes. *Appl. Phys. Lett.* **2010**, *96*, 101112.

(22) Liu, J. S.; Shan, C. X.; Li, B. H.; Zhang, Z. Z.; Yang, C. L.; Shen, D. Z.; Fan, X. W. High Responsivity Ultraviolet Photodetector Realized via a Carrier-Trapping Process. *Appl. Phys. Lett.* **2010**, *97*, 251102.

(23) Xie, X.; Zhang, Z.; Li, B.; Wang, S.; Jiang, M.; Shan, C.; Zhao, D.; Chen, H.; Shen, D. Enhanced Solar-Blind Responsivity of Photodetectors Based on Cubic MgZnO Films via Gallium Doping. *Opt. Express* **2014**, *22*, 246–253.

(24) Han, S.; Zhang, J.; Zhang, Z.; Zhao, Y.; Wang, L.; Zheng, J.; Yao, B.; Zhao, D.; Shen, D. Mg<sub>0.58</sub>Zn<sub>0.42</sub>O Thin Films on MgO Substrates with MgO Buffer Layer. *ACS Appl. Mater. Interfaces* **2010**, *2*, 1918–1921.

(25) Endo, H.; Kikuchi, M.; Ashioi, M.; Kashiwaba, Y.; Hane, K.; Kashiwaba, Y. High-Sensitivity Mid-Ultraviolet Pt/Mg<sub>0.59</sub>Zn<sub>0.41</sub>O Schottky Photodiode on a ZnO Single Crystal Substrate. *Appl. Phys. Express* **2008**, *1*, 051201.

(26) Chen, J.; Shen, W. Z. Long-Wavelength Optical Phonon Properties of Ternary MgZnO Thin Films. *Appl. Phys. Lett.* **2003**, *83*, 2154–2156.

(27) Bergman, L.; Morrison, J. L.; Chen, X.-B.; Huso, J.; Hoeck, H. Ultraviolet Photoluminescence and Raman Properties of MgZnO Nanopowders. *Appl. Phys. Lett.* **2006**, *88*, 023103.

(28) Kong, J. F.; Shen, W. Z.; Zhang, Y. W.; Yang, C.; Li, X. M. Resonant Raman Scattering Probe of Alloying Effect in ZnMgO Thin Films. *Appl. Phys. Lett.* **2008**, *92*, 191910.

(29) Vepřek, S.; Sarott, F.-A.; Iqbal, Z. Effect of Grain Boundaries on the Raman Spectra, Optical Absorption, and Elastic Light Scattering in Nanometer-Sized Crystalline Silicon. *Phys. Rev. B: Condens. Matter Mater. Phys.* **1987**, *36*, 3344.

(30) Liu, K.; Shen, D.; Shan, C.; Zhang, J.; Jiang, D.; Zhao, Y.; Yao, B.; Zhao, D. The Growth of ZnMgO Alloy Films for Deep Ultraviolet Detection. *J. Phys. D: Appl. Phys.* **2008**, *41*, 125104.

(31) Zheng, Q.; Huang, F.; Huang, J.; Hu, Q.; Chen, D.; Ding, K. Dependence of Structural and Optoelectronic Properties of Sputtered Mg<sub>0.50</sub>Zn<sub>0.50</sub>O Films on Substrate. *CrystEngComm* **2013**, *15*, 2709–2713.

(32) Choo-pun, S.; Vispute, R. D.; Yang, W.; Sharma, R. P.; Venkatesan, T.; Shen, H. Realization of Band Gap Above 5.0 eV in Metastable Cubic-Phase Mg<sub>x</sub>Zn<sub>1-x</sub>O Alloy Films. *Appl. Phys. Lett.* **2002**, *80*, 1529–1531.

(33) Takeuchi, I.; Yang, W.; Chang, K. S.; Aronova, M. A.; Venkatesan, T.; Vispute, R. D.; Bendersky, L. A. Monolithic Multichannel Ultraviolet Detector Arrays and Continuous Phase Evolution in Mg<sub>x</sub>Zn<sub>1-x</sub>O Composition Spreads. *J. Appl. Phys.* **2003**, *94*, 7336–7340.

(34) Wang, X. N.; Wang, Y.; Mei, Z. X.; Dong, J.; Zeng, Z. Q.; Yuan, H. T.; Zhang, T. C.; Du, X. L.; Jia, J. F.; Xue, Q. K. Low-Temperature Interface Engineering for High-Quality ZnO Epitaxy on Si(111) Substrate. *Appl. Phys. Lett.* **2007**, *90*, 151912.

(35) Yang, W.; Hullavarad, S. S.; Nagaraj, B.; Takeuchi, I.; Sharma, R. P.; Venkatesan, T.; Vispute, R. D.; Shen, H. Compositionally-Tuned Epitaxial Cubic Mg<sub>x</sub>Zn<sub>1-x</sub>O on Si(100) for Deep Ultraviolet Photodetectors. *Appl. Phys. Lett.* **2003**, *82*, 3424–3426.

(36) Stampe, P. A.; Bullock, M.; Tucker, W.; Kennedy, R. Growth of MgO Thin Films on M-, A-, C- and R-plane Sapphire by Laser Ablation. *J. Phys. D: Appl. Phys.* **1999**, *32*, 1778–1787.

(37) Vashaei, Z.; Minegishi, T.; Suzuki, H.; Hanada, T. Structural Variation of Cubic and Hexagonal Mg<sub>x</sub>Zn<sub>1-x</sub>O Layers Grown on MgO(111)/c-sapphire. *J. Appl. Phys.* **2005**, *98*, 054911.

(38) Razeghi, M.; Rogalski, A. Semiconductor Ultraviolet Detectors. *J. Appl. Phys.* **1996**, *79*, 7433–7473.

(39) Jiang, D.; Tian, C.; Yang, G.; Qin, J.; Liang, Q.; Zhao, J.; Hou, J.; Gao, S. Mg<sub>x</sub>Zn<sub>1-x</sub>O Solar-Blind Photodetectors Fabricated by RF Magnetron Sputtering with Combinatorial Targets. *Mater. Res. Bull.* **2015**, *67*, 158–161.

(40) Shao, D.; Yu, M.; Sun, H.; Xin, G.; Lian, J.; Sawyer, S. High-Performance Ultraviolet Photodetector Based on Organic-Inorganic Hybrid Structure. *ACS Appl. Mater. Interfaces* **2014**, *6*, 14690–14694.

(41) Fernández-Hevia, D.; de Frutos, J.; Caballero, A.; Fernández, J. Bulk-Grain Resistivity and Positive Temperature Coefficient of ZnO-Based Varistors. *Appl. Phys. Lett.* **2003**, *82*, 212–214.

(42) Grovenor, C. R. M. Grain Boundaries in Semiconductors. *J. Phys. C: Solid State Phys.* **1985**, *18*, 4079–4119.

(43) Blatter, G.; Greuter, F. Carrier Transport Through Grain Boundaries in Semiconductors. *Phys. Rev. B: Condens. Matter Mater. Phys.* **1986**, *33*, 3952–3966.

(44) Hierro, A.; Tabares, G.; Ulloa, J. M.; Muñoz, E.; Nakamura, A.; Hayashi, T.; Temmyo, J. Carrier Compensation by Deep Levels in Zn<sub>1-x</sub>Mg<sub>x</sub>O/sapphire. *Appl. Phys. Lett.* **2009**, *94*, 232101.

(45) Trunk, M.; Venkatachalapathy, V.; Galeckas, A.; Kuznetsov, A. Y. Deep Level Related Photoluminescence in ZnMgO. *Appl. Phys. Lett.* **2010**, *97*, 211901.

(46) Kim, D. C.; Kong, B. H.; Ahn, C. H.; Cho, H. K. Characteristics Improvement of Metalorganic Chemical Vapor Deposition Grown MgZnO Films by MgO Buffer Layers. *Thin Solid Films* **2009**, *518*, 1185–1189.